Electronic Supplementary Material (ESI) for Journal of Materials Chemistry A.

Supporting Information

Highly Stable 1T-MoS_2 by Magneto-hydrothermal Synthesis with Ru Modification for Efficient Hydrogen Evolution Reaction

Lili Zhu,‡[ab] Zheng Wang,‡[c] Changdian Li,[ab] Han Li,[ab] Yanan Huang,[a] Hui Li,[ab] Ziqiang Wu,[ab] Shuai Lin,[a] Neng Li,*[cd] Xuebin Zhu*[ab] and Yuping Sun[a,e,f]

[a] Key Laboratory of Materials Physics, Institute of Solid State Physics, HFIPS, Chinese Academy of Sciences, Hefei 230031, China

[b] University of Science and Technology of China, Hefei 230026, China

[c] State Key Laboratory of Silicate Materials for Architectures, Wuhan University of Technology, Hubei 430070, China

[d] State Center for International Cooperation on Designer Low-Carbon & Environmental Materials (CDLCEM), School of Materials Science and Engineering, Zhengzhou University, Zhengzhou 450001, China

[e] High Magnetic Field Laboratory, HFIPS, Chinese Academy of Sciences, Hefei 230031, China

[f] Collaborative Innovation Center of Advanced Microstructures, Nanjing University, Nanjing 210093, China

***Corresponding authors E-mail:** lineng@whut.edu.cn; xbzhu@issp.ac.cn

‡The two authors contributed equally to this work.

List of Texts, Figures and Tables

(c) Ru 3*p* XPS spectra, (d) Mo 3*d* XPS spectra and (e) S 2*p* XPS spectra of 1T-MoS_2 and Ru/1T-MoS_2.

Table S1. ICP measurements of element content for Ru/1T-MoS_2 catalysts [wt.%].

Fig. S11 Static contact angle images of Ru/2H-MoS_2.

Fig. S12 EIS of Ru/1T-MoS_2 at different overpotentials (inset: the equivalent electrical circuit to model HER process).

Fig. S13 CV curves of (a) Ru/1T-MoS_2 and (b) Ru/2H-MoS_2 at the potential range of 0.05-0.25 V vs. RHE with the scanning rates of 20, 40, 60, 80 and 100 mV s^{-1}, respectively.

Table S2 The ECSAs of different as-prepared electrocatalysts in this work.

Fig. S14 The stability test of the chronoamperometric test for 168 h.

Fig. S15 (a) TEM image, (b) HRTEM image, (c) HAADF-STEM image, (d-f) EDX element mapping of Ru, Mo and S of Ru/1T-MoS_2 after stability test. The high-resolution XPS results for (g) Ru 3*p*, (h) Ru 3*d* and C 1*s*, (i) Mo 3*d* and (j) S 2*p* of Ru/1T-MoS_2 electrode with initial and after stability test.

Fig. S16 (a) LSV curves and (b) Tafel plots with the mass activity for 20 wt% Pt/C, Ru/1T-MoS_2, Ru/2H-MoS_2, 1T-MoS_2 and 2H-MoS_2 for HER; (c) LSV curves and (d) Tafel plots with the mass activity for 20 wt% Pt/C, MoS_2-9T, MoS_2-5T, MoS_2-3T and MoS_2-0T for HER.

Fig. S17 Ru nanoparticles on MoS_2 (002) surfaces of the two load sites : (a) site 1, (b) site 2. Brown and yellow are used to distinguish the upper and lower sulfur atoms.

Fig. S18 (a) and (b) Ru nanoparticles anchored on 2H-MoS_2; (c) and (d) Ru

nanoparticles anchored on 1T-MoS_2.

Fig. S19 Hydrogen is adsorbed on (a) and (b) 2H-MoS_2; (c) and (d)1T-MoS_2; (e) and (f) Ru/2H-MoS_2; (g) and (h) Ru/1T-MoS_2.

Fig. S20 Electronic structure of Ru nanoparticles on the surface of 2H-MoS_2.

Fig. S21 On the surface of (a) 1T-MoS_2, (b) 2H-MoS_2, d_z^2 orbitals of Ru nanoparticles are bonded between the *s* orbitals of H.

Fig. S22 Charge density difference: (a) 2H-MoS_2, (b) 1T-MoS_2, (c) Ru/2H-MoS_2, (d) Ru/1T-MoS_2.

Fig. S23 Vibration of energy against time in AIMD simulation of (a) Ru/2H-MoS_2 and (c) Ru/1T-MoS_2 under 300 K with the time step of 1 fs. Side view of (b) Ru/2H-MoS_2 and (d) Ru/1T-MoS_2 monolayer after the AIMD simulation.

Table S3 Comparisons of various metal modified TMDs composites used as catalysts in 0.5 M H_2SO_4 for HER performances.

1. Experimental and theoretical sections

1.1. Chemicals

$(NH_4)_6Mo_7O_{24}\cdot 4H_2O$ and thiourea were purchased from Alfa Aesar. Purchase of $RuCl_3\cdot xH_2O$ (35.0-42.0% Ru basis) from Aladdin Industrial Company. Purchase of Nafion (5 wt%) and 20 wt% Pt/C catalyst from Sigma-Aldrich Company. Other reagents were analytically pure and had not been purified furtherly. Deionized water was used during whole experiment.

1.2. Synthesis of MoS_2 and Ru/MoS_2

$(NH_4)_6Mo_7O_{24}\cdot 4H_2O$ and thiourea were dissolved in deionized water, and the homogeneous solution was obtained by ingenious stirring. After the mixture was transferred to a Teflon autoclave (capacity of 28 mL), magnetic field was utilized. Then heated to 210 °C for 40 minutes, keeping 18 hours under different magnetic fields. 1T-1T-MoS_2 and 2H-MoS_2 were produced at magnetic field of 9T and 0T, respectively. Synthesized products were rinsed by ethanol and deionized water, centrifuged a few times, finally stored in vacuum under 70 °C.

Ru/1T-MoS_2 catalyst (the theoretical and experimental value of Ru is 7.5 wt %) was prepared by chemical reduction method, and 1T-MoS_2 was stirred with the required amount of $RuCl_3$ aqueous solution for 30 minutes to form $RuCl_3$/1T-MoS_2 (ca. 10 mL), then, dried in vacuum overnight. Afterwards, the above dried powder was reduced by 0.1 M NaOH/0.1 M $NaBH_4$ mixed solution. The product was rinsed by ethanol and deionized water, centrifuged a few times, finally stored in vacuum under 50 °C. The synthesis method of Ru/2H-MoS_2 was the same as that of Ru/1T-MoS_2, beyond that 1T-

MoS_2 was replaced by 2H-MoS_2.

1.3. Characterization

Scanning electron microscope (SEM) and transmission electron microscope (TEM) images were captured in Quanta 200FEG SEM and JEM-2100 TEM, respectively. Raman spectroscopy was analyzed with a LabRAMHR800 UV near-infrared spectrometer excited by the laser of 532 nm. Philips X'pert PRO performed X-ray diffraction (XRD). Contact angle of water at room temperature was measured by static drop technique. Place water drops on the surface of cold-pressed sample plate. Contact angle was measured by the photos which were taken by CCD camera, and the precision is about ± 2 °. X-ray photoelectron spectroscopy (XPS) was realized on Thermo Scientific K-Alpha device, and the excitation source is Al K_α. Elemental intensities were tested by the inductively coupled plasma mass spectrometer (ICP-MS) with instrument model of Thermo Fisher iCAP RQ.

1.4. Electrochemical testing

4 mg catalyst was put in 100 μL 0.5 wt % Nafion solution and 1 mL 5: 1 (*V* / *V*) water-isopropyl, ultrasonic stirring for 30 minutes to form ink. 6 μL disperse was loaded on glassy carbon electrode (GCE) (diameter of 3 mm) (loading mass ~ 0.31 mg cm^{-2}).

Room temperature electrochemical testing of 0.5 M H_2SO_4 electrolyte was performed by regular three-electrode cell and nitrogen gas flow system on CHI660E workstation. GCE, graphite rod and Ag/AgCl electrode with 3 M KCl solution were utilized as corresponding working electrode, counter electrode and reference electrode. Calibrating all potentials on reversible hydrogen electrode (RHE) to obtain

overpotential, according to E (*vs.* RHE) = E (*vs.* Ag/AgCl) + $E_{Ag/AgCl}$ + 0.0591 pH. Linear scanning voltammetry (LSV) was utilized and scanning rate was 5 mV s^{-1} with 95 % *iR* compensation (The iR compensation used in this electrochemical test is automatic compensation by electrochemical workstation. 95% iR compensation is used instead of 100%, because 100% iR compensation may lead to instrument resonance and large error in test data.). A sequence of cycle voltammetry (CV) tests were carried out with scanning rates of 20 to 100 mV s^{-1}, double-layer capacitance (C_{dl}) and electrochemical active surface area (ECSA) were calculated. Under 120, 140, 160, 180 and 200 mV (*vs.* RHE), electrochemical impedance spectroscopy (EIS) with 5 mV amplitude was obtained in frequency region of 0.1 to 10^5 Hz. Chronoamperometric test was performed for 24 hours.

1.5. Theoretical part

Spin-polarized density functional theory (DFT) was calculated by the Vienna *ab initio* simulation package (VASP) [1, 2]. The pseudopotentials adopted the projector augmented wave (PAW) methods [3]. Generalized gradient approximation (GGA) with the Perdew-Burke-Emzerhof (PBE) [4] functionals was [1]used to describe the exchange-correlation energy. Energy cutoff for plane-wave basis was 400 eV, and the convergence threshold for geometry relaxation was 10^{-5} eV in energy and 0.02 eV $Å^{-1}$ in force. The van der Waals interaction was considered by DFT-D3 method [5]. With 3 × 3 × 1 and 5 × 5 × 1 grid as the center, *k*-points in Brillouin zone were sampled for structural optimization and static self-consistent calculations respectively. Beder charge analysis [6] was used to study electron transfer between adjacent atoms.

In catalytic reactions, the ease of the reactions is generally evaluated by calculating the magnitude of the Gibbs free energy change (ΔG) as well as the positive and negative. The Gibbs free energy has the following formula:

$$G(T) = E_{DFT} + E_{ZPE} + U(T) - TS \text{ [7]} \qquad (1)$$

where T = 298.15 K, E_{DFT} is the energy output after VASP calculation, E_{ZPE} is zero-point energy, U is internal energy of the system, and S is the entropy.

2. Preparation and characterization of MoS_2 with different 1T phase content

2.1. Morphology of MoS_2 with different 1T phase content

By deconvoluting the XPS peaks (Fig. 1c), the percentage of 1T-MoS_2 synthesized under 0, 3, 5 and 9 T is, respectively, estimated to be 25, 38, 50 and 100% (Fig. S1a). The morphology of as-synthesized MoS_2 under 0, 3, 5 and 9 T was characterized by scanning electron microscope (SEM) (Fig. S1b-e). The four synthesized MoS_2 samples are composed of nanosheets with the corrugated and wavy graphene-like morphology. In addition, a drop of water (2 μL) can be dropped on the cold pressed sample to measure contact angle and estimate the hydrophilicity. Contact angles of MoS_2-0T, MoS_2-3T, MoS_2-5T and MoS_2-9T (Fig. S2a-d) are 45, 39, 32 and 22 °, respectively, indicating that 1T-MoS_2 has the best hydrophilicity.

2.2. HER activity of MoS_2 with different 1T phase content

The successful preparation of MoS_2 multilayer nanosheets at four different magnetic field (MF) intensities may be explored the electrochemical properties, especially for pure 1T-MoS_2 multilayer nanosheets prepared at the MF of 9T with high environmental stability. The properties of the obtained MoS_2 samples as an HER electrocatalyst were

evaluated in 0.5 M H_2SO_4 electrolyte.

LSV curves (Fig. S4a) indicate overpotential for thermodynamic behavior of the as-prepared electrocatalysts. The occurrence of initial overpotential (η_{onset}) (corresponding to 1 mA cm^{-2}) and the potential of 10 mA cm^{-2} (η_{10}) are 10 and 47 mV separately for 20 wt% Pt/C regarded as HER benchmark electrocatalyst, which is in accordance with the reportorial results. η_{onset} of MoS_2-9T, MoS_2-5T, MoS_2-3T and MoS_2-0T correspond to 122, 125, 130 and 197 mV. η_{10} of MoS_2-9T, MoS_2-5T, MoS_2-3T and MoS_2-0T are 189, 212, 233 and 286 mV, respectively. Obviously, MoS_2-9T has the lowest overpotential, indicating that MoS_2-9T (1T-MoS_2) has the best HER performance among the four electrocatalysts.

Tafel plots obtained from LSV curves are displayed in Fig. S4b, allowing for the kinetic behavior of the electrocatalyst. Notably, the corresponding Tafel slopes of MoS_2-9T, MoS_2-5T, MoS_2-3T, and MoS_2-0T are 58, 63, 65 and 66 mV dec^{-1}, suggesting the Volmer-Heyrovsky mechanism [8]. Electrochemical desorption is the rate-limiting step. Tafel slope of 20 wt% Pt/C for HER testing is 30 mV dec^{-1} that is close to the results of literature [9]. Fig. S4c displays the overpotentials of the electrocatalyst under different current densities and Tafel slopes, which notarizes that 1T-MoS_2 has superior HER performance.

EIS technology is a vital technology to study the kinetic process of electrocatalyst. According to the Nyquist diagram and the equivalent circuit (Fig. S4d), MoS_2-9T owns the lowest charge transfer resistance (R_{ct}) of approximate 130 Ω, indicating that MoS_2-9T has the best inherent conductivity, which is consistent in the superior HER activity

among these samples. As can be seen from Fig. S5, MoS_2-9T electrocatalyst is tested EIS at different overpotentials, and it is obvious that the R_{ct} value decreases along with overpotential from 120 to 200 mV. The results show 1T-MoS_2 electrocatalyst possesses an eminent electron transfer capability at upper overpotential.

In addition, for MoS_2 with various MF intensities, the effective ECSA of each electrocatalyst is directly proportional to C_{dl} calculated by CV tests (Fig. S6a-d). The corresponding C_{dl} value (Fig. S4e) of MoS_2-9T, MoS_2-5T, MoS_2-3T and MoS_2-0T are 37.75, 31.59, 18.94 and 4.25 mF cm^{-2}. The results display that 1T-MoS_2 owns the highest electrochemical active surface area.

To assess stability, chronoamperometric test was performed on MoS_2-9T electrocatalysts. Remarkable long-term electrochemical stability is proved by 24 hours of stability test (Fig. S4f). These electrochemical test results clearly indicate that MoS_2 has HER activity and MoS_2-9T (1T-MoS_2) possesses excellent HER performance.

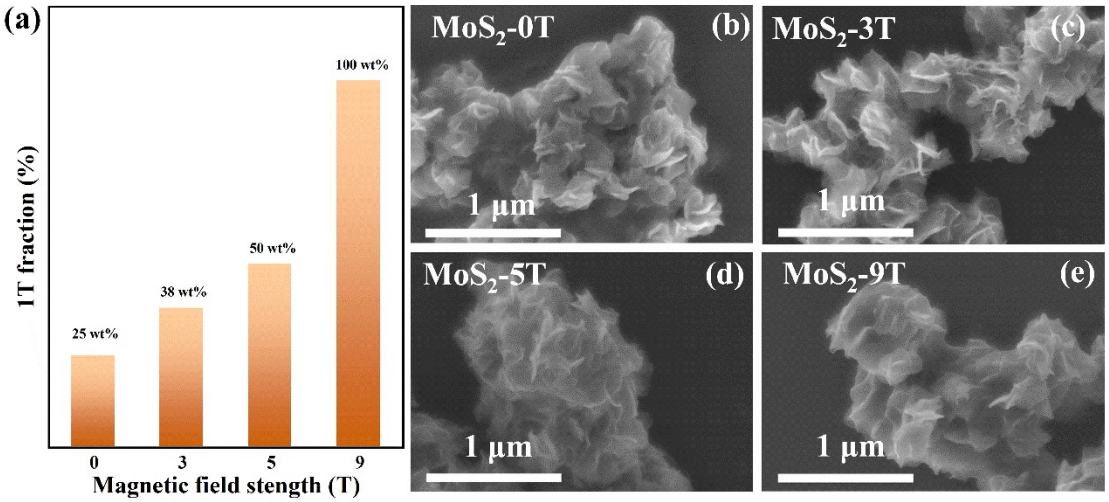

Fig. S1 (a) 1T phase percentage of mixed phase of MoS_2; SEM images of (b) MoS_2-0T, (c) MoS_2-3T, (d) MoS_2-5T and (e) MoS_2-9T.

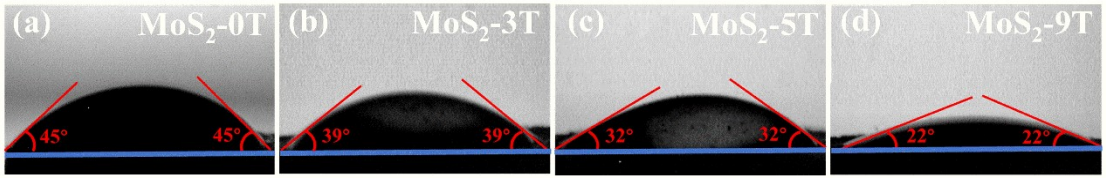

Fig. S2 (a-d) Static contact angle images of MoS_2-0T, MoS_2-3T, MoS_2-5T and MoS_2-9T, respectively.

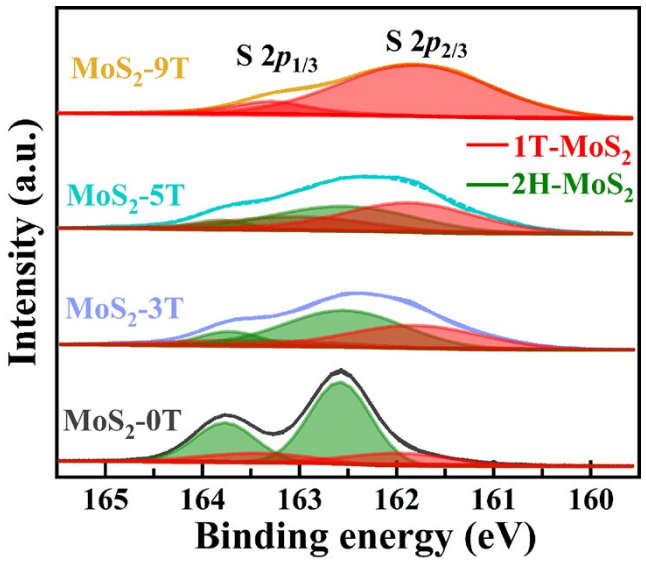

Fig. S3 XPS results from S 2*p* region of the MoS_2 obtained at various magnetic fields intensities.

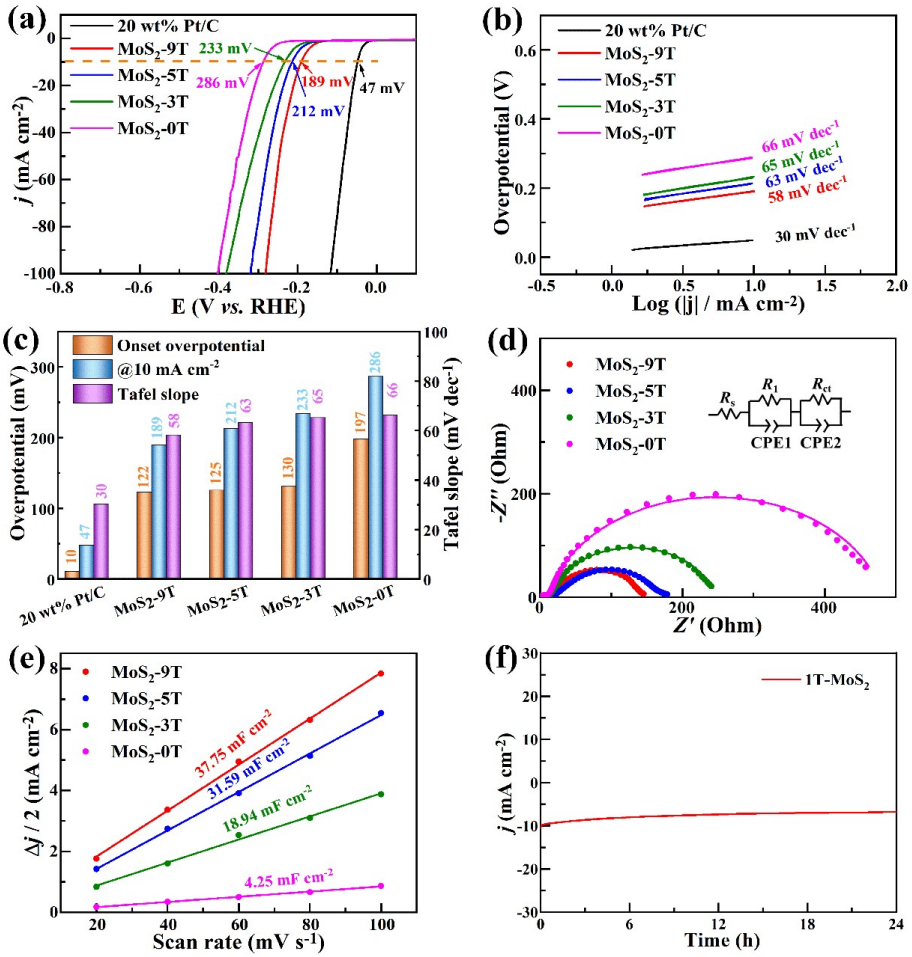

Fig. 4 (a) LSV curves of HER for MoS_2-0T, MoS_2-3T, MoS_2-5T, MoS_2-9T and 20 wt% Pt/C. (b) Tafel plots. (c) Comparisons of the η_{onset}, η_{10} and Tafel slope of various samples. (d) EIS of MoS_2-0T, MoS_2-3T, MoS_2-5T, MoS_2-9T (inset: equivalent electrical circuit). (e) Plots of C_{dl} for MoS_2-0T, MoS_2-3T, MoS_2-5T, MoS_2-9T. (f) Chronoamperometric test of HER at 10 mA cm^{-2} using 1T-MoS_2 as catalyst.

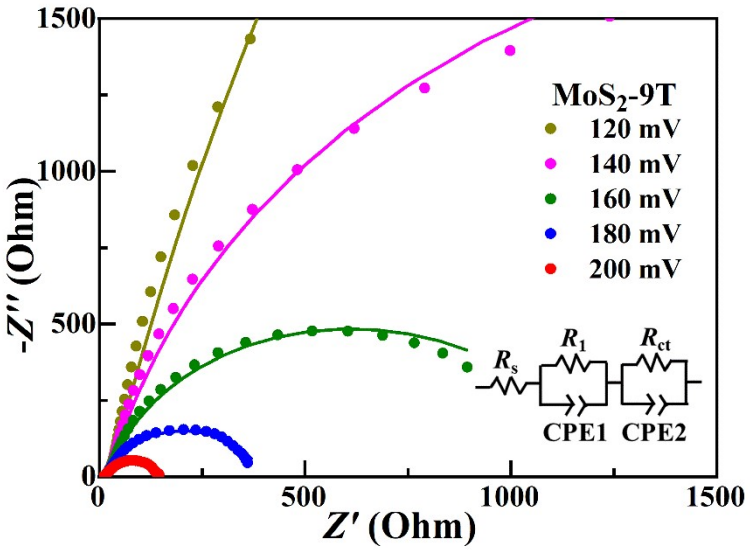

Fig. S5 EIS of MoS_2-9T at different overpotentials (inset: the equivalent electrical circuit to model HER process).

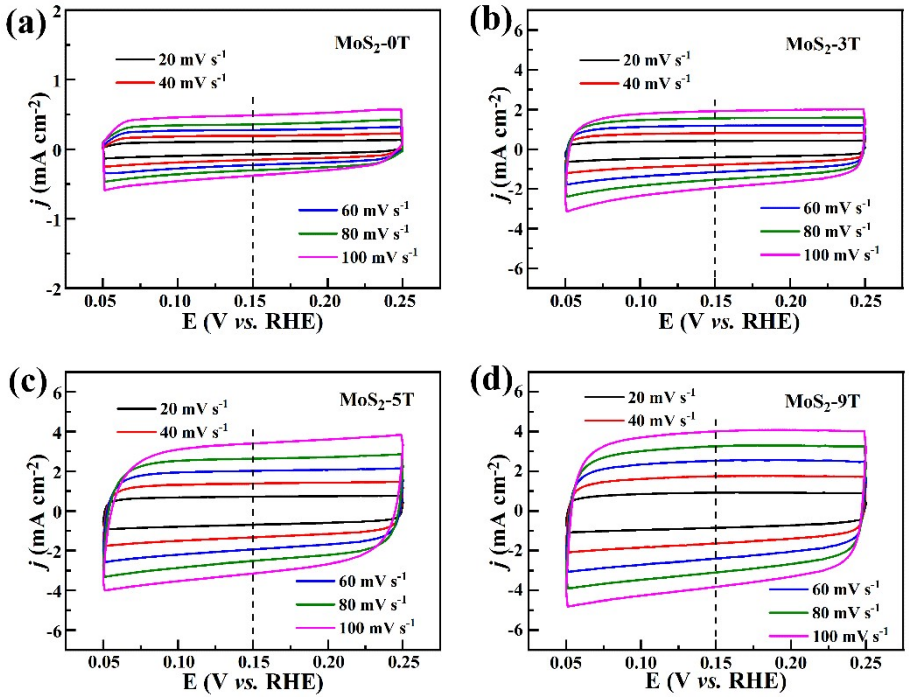

Fig. S6 CV curves of (a) MoS_2-0T, (b) MoS_2-3T, (c) MoS_2-5T and (d) MoS_2-9T at the potential range of 0.05-0.25 V vs. RHE with the scanning rates of 20, 40, 60, 80 and 100 mV s^{-1}, respectively.

MoS_2 nanosheets have been partially oxidized by saturating the MoS_2 solution with oxygen in a few days for edge oxidation. As shown in Figure R6，the oxidation of the edges leads to the drastic reduction in electrochemical catalytic activity for 2H-MoS_2 nanosheets, however, the catalytic performance is slightly affected by oxidation for 1T phase of MoS_2 nanosheets, manifesting that the basal plane is main catalytically active sites for 1T-MoS_2 and edges of nanosheets is active sites for 2H-MoS_2.

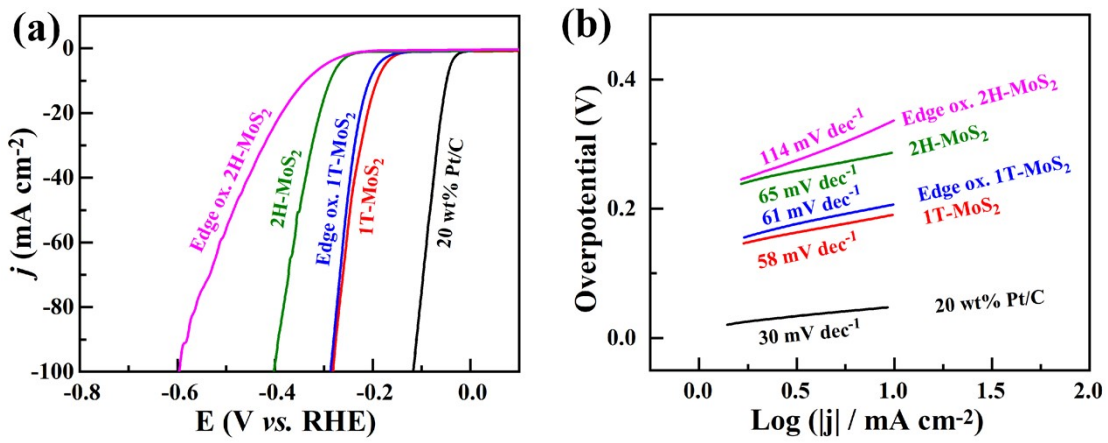

Fig. S7 HER activity of MoS_2 nanosheets. (a) Polarization curves of 1T-MoS_2 and 2H-MoS_2 nanosheet before and after edge oxidation. (b) Corresponding Tafel plots.

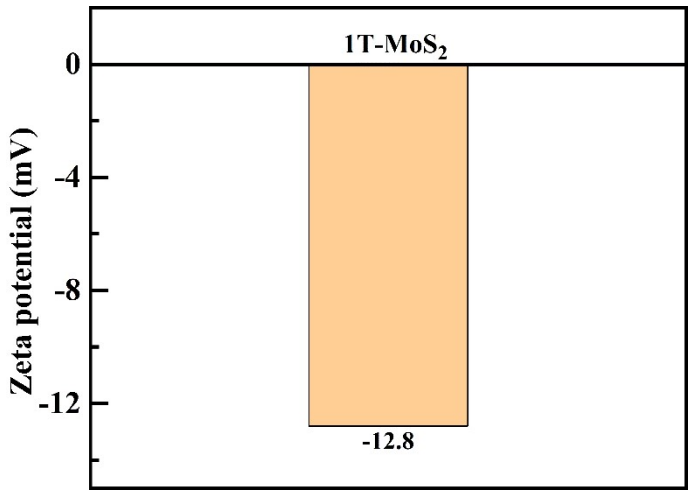

Fig. S8 Zeta potential of 1T-MoS_2 that is dispersed in water at pH of 7.

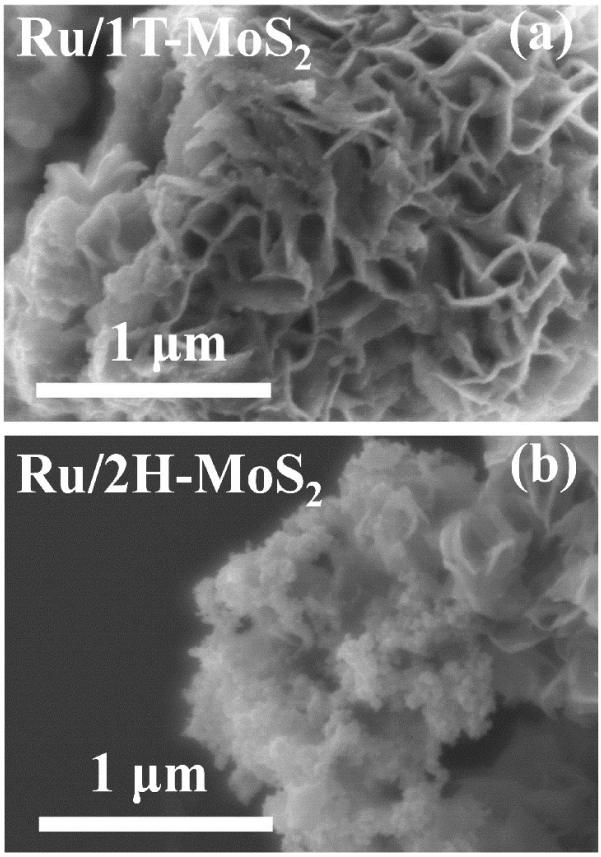

Fig. S9 SEM images of (a) Ru/1T-MoS_2 and (c) Ru/2H-MoS_2.

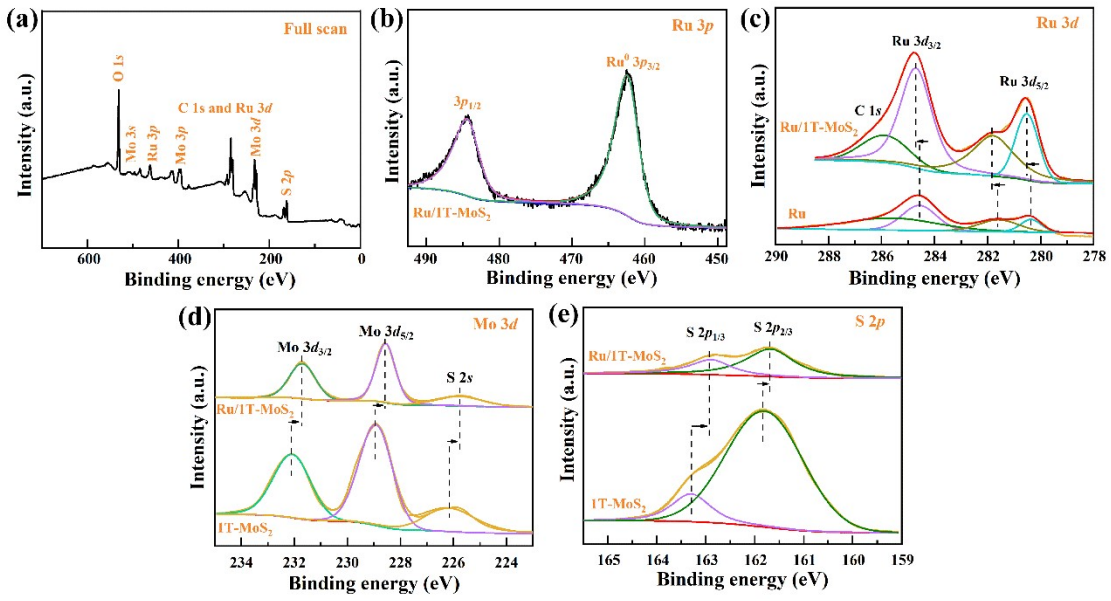

Fig. S10 XPS characterizations: (a) survey and (b) Ru 3*p* XPS spectra of Ru/1T-MoS_2; (c) Ru 3*p* XPS spectra, (d) Mo 3*d* XPS spectra and (e) S 2*p* XPS spectra of 1T-MoS_2 and Ru/1T-MoS_2.

The loading contents of the Ru species have been confirmed by the ICP-MS, the results of element content for Ru/1T-MoS_2 is present in Table S1 and the loading content of Ru species is 9.34 wt.%.

Table S1. ICP measurements of element content for Ru/1T-MoS_2 catalysts [wt.%].

Element / Catalyst	Ru (wt.%)	Mo (wt.%)	S (wt.%)
Ru/1T-MoS_2	9.34	31.60	59.06

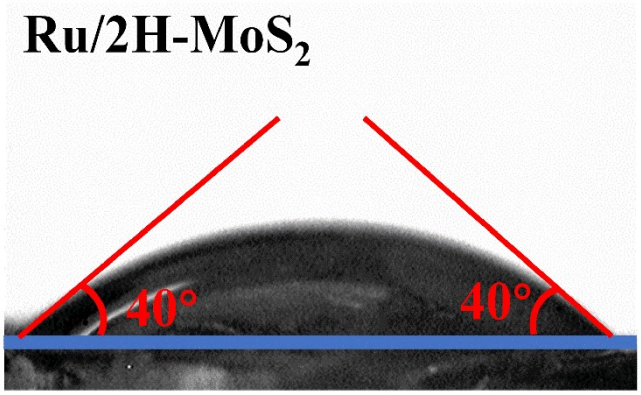

Fig. S11 Static contact angle images of Ru/2H-MoS_2.

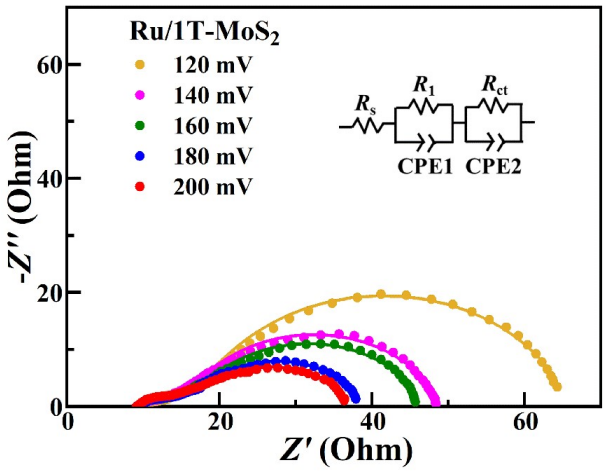

Fig. S12 EIS of Ru/1T-MoS_2 at different overpotentials (inset: the equivalent electrical circuit to model HER process).

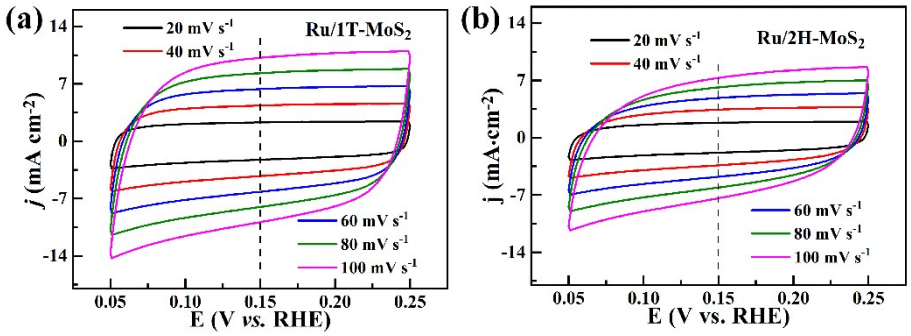

Fig. S13 CV curves of (a) Ru/1T-MoS_2 and (b) Ru/2H-MoS_2 at the potential range of 0.05-0.25 V vs. RHE with the scanning rates of 20, 40, 60, 80 and 100 mV s^{-1}, respectively.

Electrochemical surface area (ECSA)

$A_{ECSA} = C_{dl} / (C_s \text{ per ECSA cm}^2)$

C_s is the specific capacitance of atomically smooth planar surface in respective electrolytic medium [10]. In this work, C_s was considered to be 35 μF cm^{-2} for 0.5 M H_2SO_4 [11].

Table S2. The ECSAs of different as-prepared electrocatalysts in this work.

Electrocatalysts	C_{dl} (mF cm^{-2})	ECSA (cm^2)
MoS_2-0T (2H-MoS_2)	4.25	121.43
MoS_2-3T (2H/1T-MoS_2)	18.94	541.14
MoS_2-5T (2H/1T-MoS_2)	31.59	902.57

MoS_2-9T ($1T$-MoS_2)	37.75	1078.57
Ru/2H-MoS_2	69.15	1975.71
Ru/1T-MoS_2	97.53	2786.57

The catalytic stability of Ru/1T-MoS_2 at initial current density of 10 mA cm^{-2} in 0.5 M H_2SO_4 for 168 hours has been tested. After 168-hour stability test, the current density retention for Ru/1T-MoS_2 remains 38.49%, which shows that the prepared electrocatalyst is relatively robust (Fig. S14).

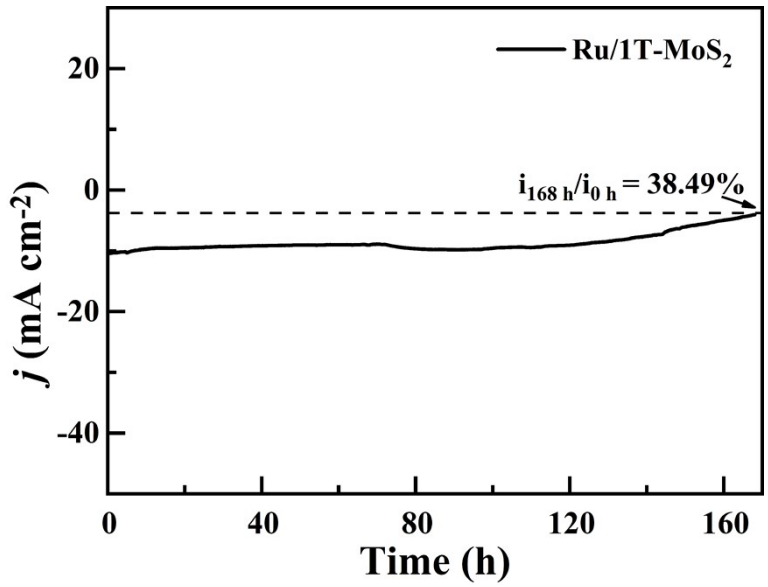

Fig. S14 The stability test of the chronoamperometric test for 168 h.

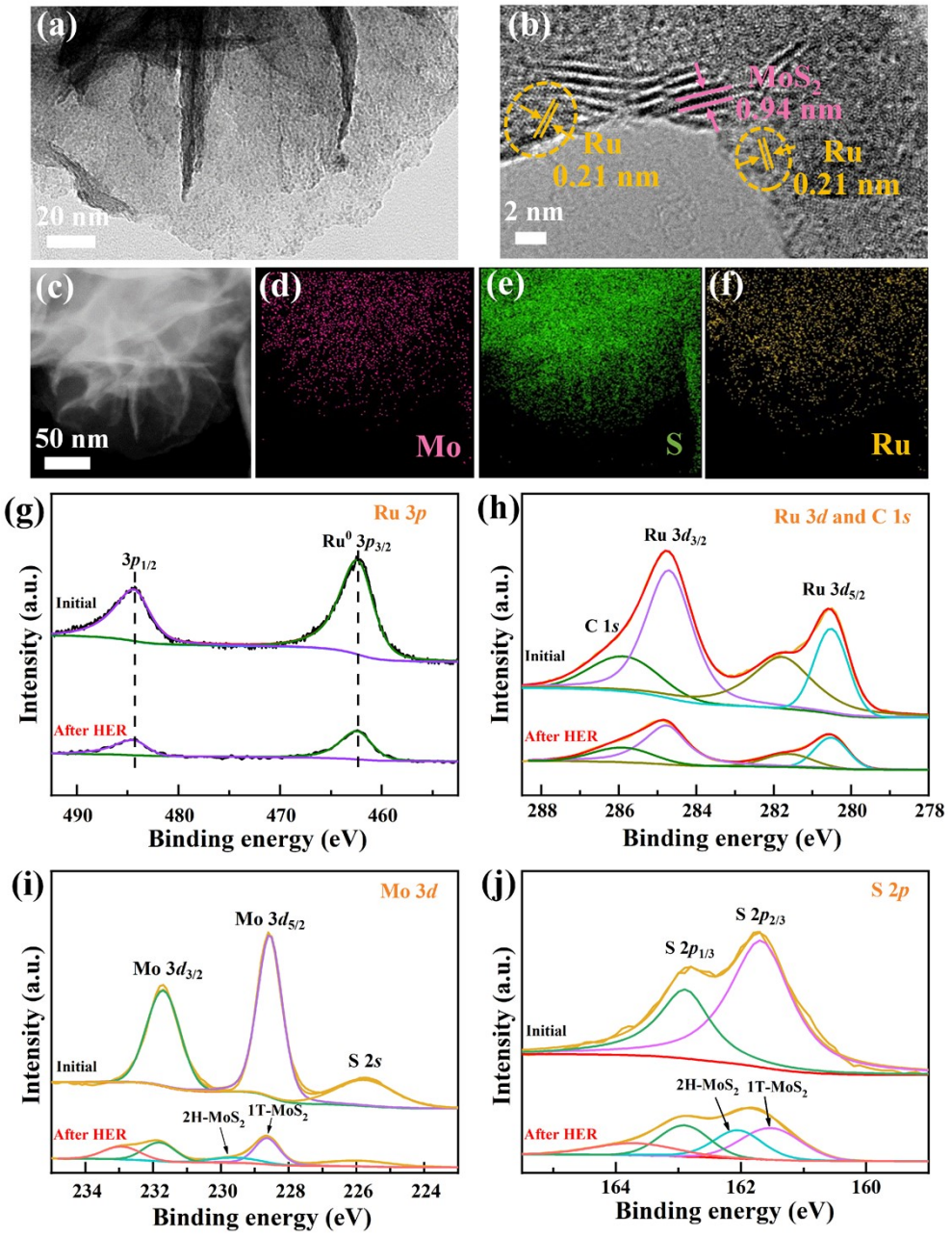

Fig. S15 (a) TEM image, (b) HRTEM image, (c) HAADF-STEM image, (d-f) EDX element mapping of Ru, Mo and S of Ru/1T-MoS_2 after stability test. The high-resolution XPS results for (g) Ru 3*p*, (h) Ru 3*d* and C 1*s*, (i) Mo 3*d* and (j) S 2*p* of Ru/1T-MoS_2 electrode with initial and after stability test.

The mass activity of the as-prepared catalysts has been calculated to reflect the

intrinsic catalytic property of these catalysts (Fig. S16).

The LSV curves of HER mass activity are shown in the Fig. S16a and Fig. S16c. The overpotential of 10 mA mg-1 catalyst for 20 wt% Pt/C, Ru/1T-MoS_2, Ru/2H-MoS_2, MoS_2-9T (1T-MoS_2), MoS_2-5T, MoS_2-3T and MoS_2-0T (2H-MoS_2) is 34, 54, 82, 163, 184, 199 and 258 mV, respectively. Correspondingly, the Tafel slope of 20 wt% Pt/C, Ru/1T-MoS_2, Ru/2H-MoS_2, MoS_2-9T (1T-MoS_2), MoS_2-5T, MoS_2-3T and MoS_2-0T (2H-MoS_2) is 33, 53, 55, 56, 60, 63 and 64 mV dec^{-1}, respectively.

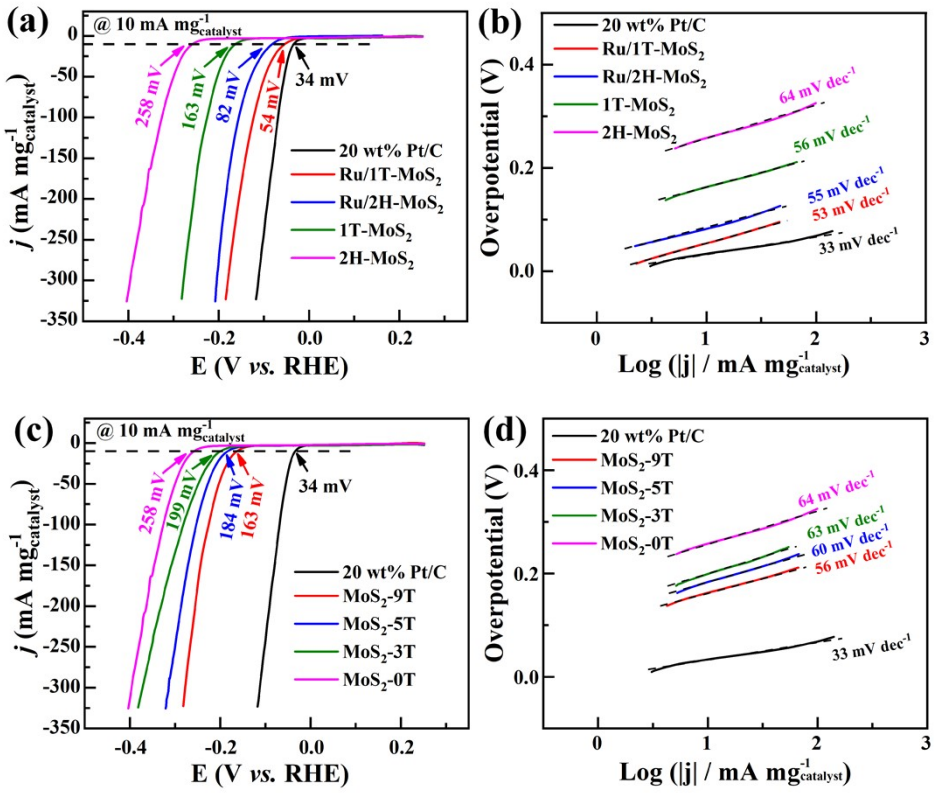

Fig. S16 (a) LSV curves and (b) Tafel plots with the mass activity for 20 wt% Pt/C, Ru/1T-MoS_2, Ru/2H-MoS_2, 1T-MoS_2 and 2H-MoS_2 for HER; (c) LSV curves and (d) Tafel plots with the mass activity for 20 wt% Pt/C, MoS_2-9T, MoS_2-5T, MoS_2-3T and MoS_2-0T for HER.

The viable model is proposed to account for the interaction effects between Ru and 1T-MoS_2, which estimates the effect of their interaction for electrocatalytical HER performance. The hexagonal MoS_2 structure was chosen for the modeling, where the space group of the 2H phase is $P6_3/mmc$ and the space group of the 1T phase is Pm1. To simulate the experimental loading of Ru clusters on the MoS_2 (002) surface, a MoS_2 3×3 supercells was built and then a tetrahedral cluster consisting of four Ru atoms was loaded on its (002) surface. Fig. S17 shows that Ru clusters have two loading sites on the MoS_2 (002) surface: site 1 and site 2. Site 2 has lower energy by calculation, while AIMD simulations at 300 K verified their structural stability. A vacuum space of 20 Å was introduced in the z direction in all structures to avoid interlayer interference of MoS_2 due to the crystal period structure.

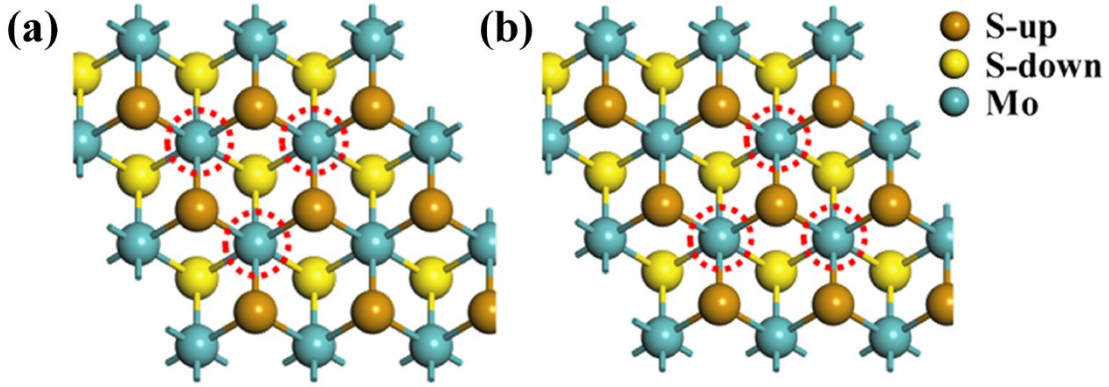

Fig. S17 Ru nanoparticles on MoS_2 (002) surfaces of the two load sites : (a) site 1, (b) site 2. Brown and yellow are used to distinguish the upper and lower sulfur atoms.

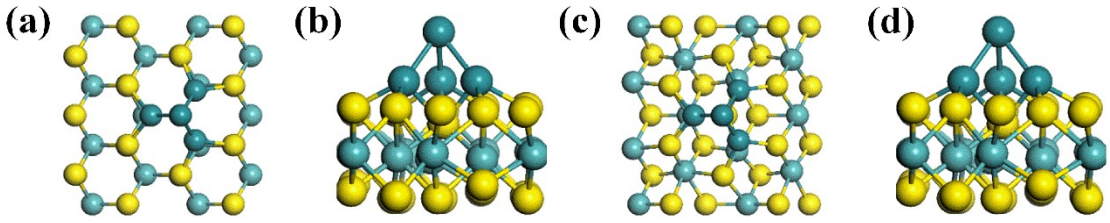

Fig. S18 (a) and (b) Ru nanoparticles anchored on 2H-MoS_2; (c) and (d) Ru

nanoparticles anchored on 1T-MoS_2.

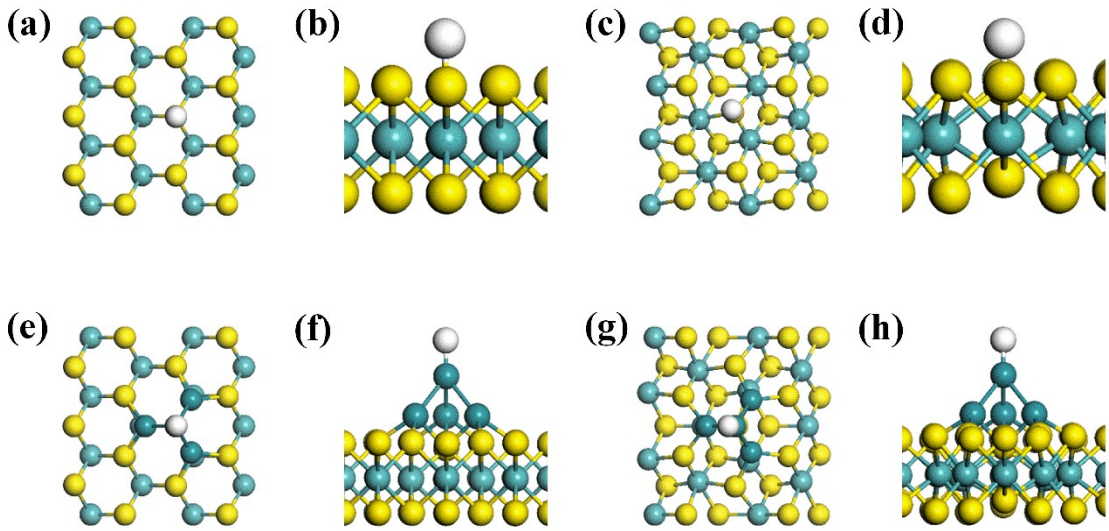

Fig. S19 Hydrogen is adsorbed on (a) and (b) 2H-MoS_2; (c) and (d)1T-MoS_2; (e) and (f) Ru/2H-MoS_2; (g) and (h) Ru/1T-MoS_2.

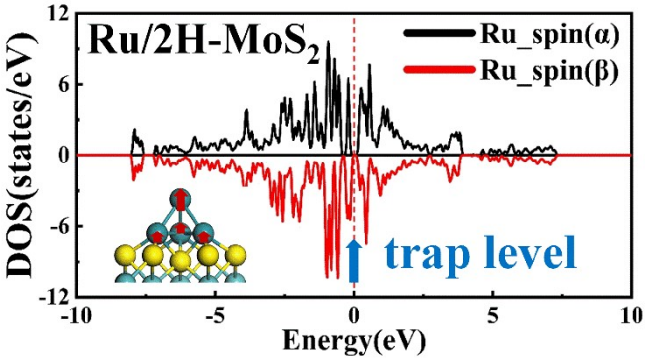

Fig. S20 Electronic structure of Ru nanoparticles on the surface of 2H-MoS_2.

Ru nanoparticles on the surface of 2H-MoS_2 exhibit strong magnetic properties while Ru NPs on the surface of 1T-MoS_2 exhibit weak non-magnetic properties. The d_{z^2} orbitals of the weakly magnetic Ru on the surface of 1T-MoS_2 (Fig. S21a) exhibit more off-domain coupling into bonds with the *s* orbitals of H than the strongly magnetic Ru NPs on the surface of 2H-MoS_2 (Fig. S21b). Moreover, the strongly magnetic Ru causes

an energy level mismatch in the density of states of different spin states of the *s* orbitals of H. This energy level mismatch has a bad effect on the HER reaction efficiency.

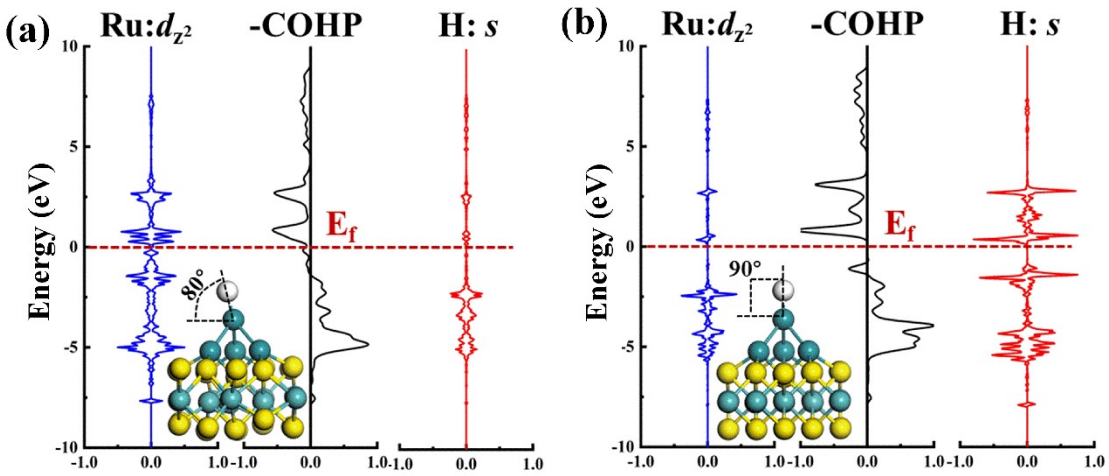

Fig. S21 On the surface of (a) 1T-MoS_2, (b) 2H-MoS_2, d_z^2 orbitals of Ru nanoparticles are bonded between the *s* orbitals of H.

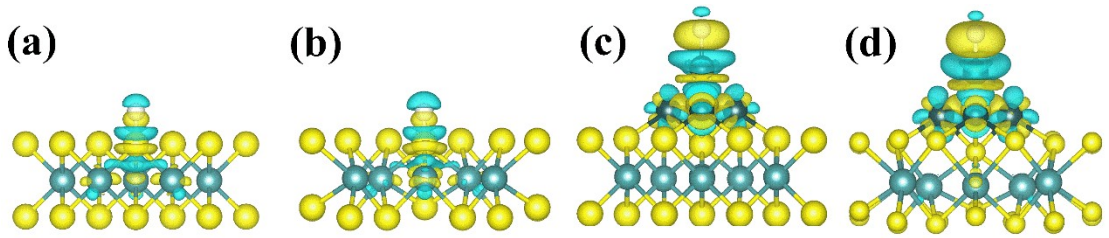

Fig. S22 Charge density difference: (a) 2H-MoS_2, (b) 1T-MoS_2, (c) Ru/2H-MoS_2, (d) Ru/1T-MoS_2.

To verify the stability of Ru/2H-MoS_2 (Fig. S23a-b) and Ru/1T-MoS_2 (Fig. S23c-d), the NVT ensemble AIMD simulation is performed at 300 K for 10 ps. Energy oscillates slightly near the equilibrium configuration after a period, and no notable geometric deformation is found, suggesting the excellent stability of Ru/1T-MoS_2.

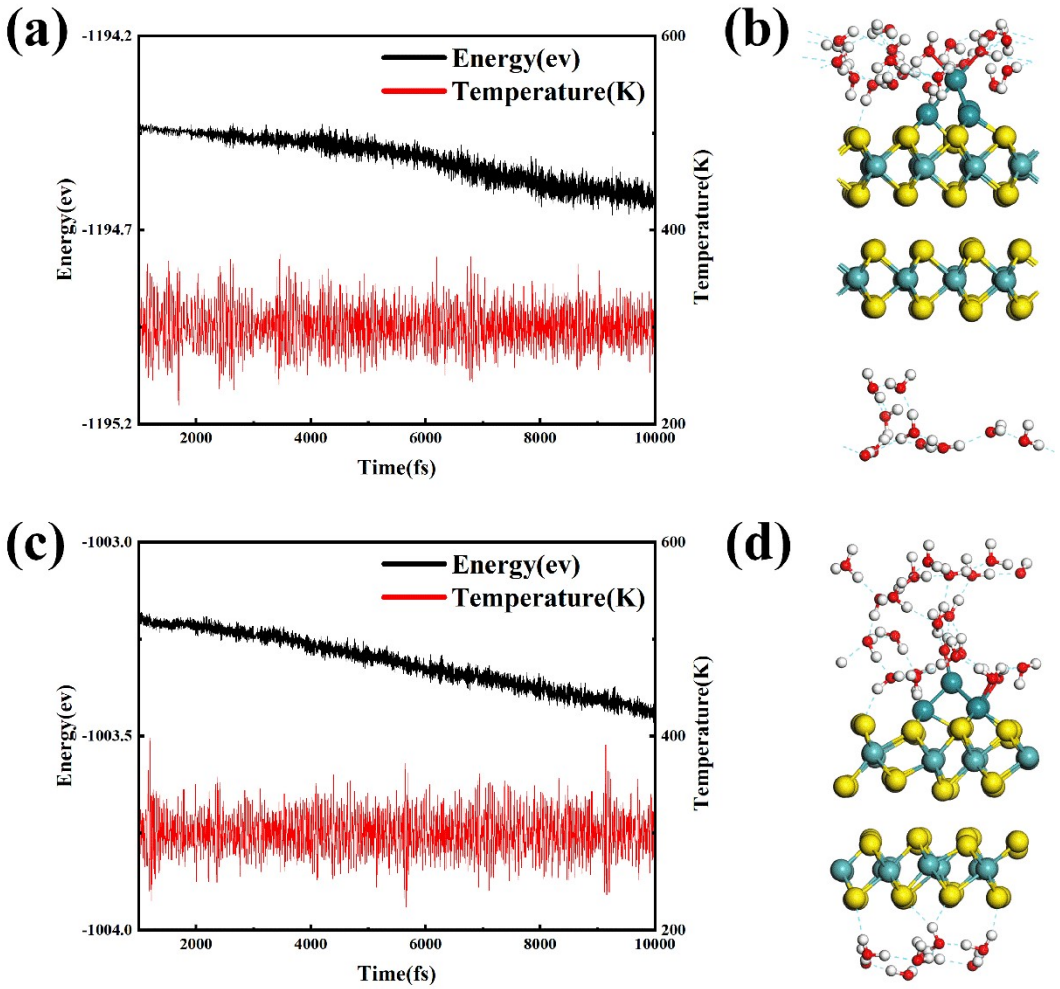

Fig. S23 Vibration of energy against time in AIMD simulation of (a) Ru/2H-MoS_2 and (c) Ru/1T-MoS_2 under 300 K with the time step of 1 fs. Side view of (b) Ru/2H-MoS_2 and (d) Ru/1T-MoS_2 monolayer after the AIMD simulation.

Table S3. Comparisons of various metal modified TMDs composites used as catalysts in 0.5 M H_2SO_4 for HER performances.

Catalysts	Overpotential at 10 mA cm^{-2} (mV)	Tafel slope (mV dec^{-1})	iR compensation	References
Ru/1T-MoS_2	81	54	95 % iR compensation	This work
1T-MoS_2	189	58		

2H-MoS_2	286	66		
5.2 wt% Rh-MoS_2	47	24	Without iR compensation	[12]
Rh-MoS_2	67	54	Without iR compensation	[13]
Pt-MoS_2	86	41	Without iR compensation	[14]
Pd-$MoS_{2-x}N_y$/rGO	93	58	With iR compensation	[15]
Ru/MoS_2	96	60	With iR compensation	[16]
Ru-MoS_2	100	46	-	[17]
Cu@MoS_2	131	51	-	[18]
Au@MoS_2	164	50	Without iR compensation	[19]
Zn@MoS_2	194	73	-	[20]

References

[1] G. Kresse, J. Furthmuller, *Comp. Mater. Sci.*, 1996, **6**, 15-50.

[2] G. Kresse, J. Furthmuller, J. Hafner, *Phys. Rev. B*, 1994, **50**, 13181-13185.

[3] P.E. Blochl, *Phys. Rev. B*, 1994, **50**, 17953-17979.

[4] J.P. Perdew, J.A. Chevary, S.H. Vosko, K.A. Jackson, M.R. Pederson, D.J. Singh, C. Fiolhais, *Phys. Rev. B*, 1992, **46**, 6671-6687.

[5] S. Grimme, J. Antony, S. Ehrlich, H. Krieg, *J. Chem. Phys.*, 2010, **132**, 154104.

[6] W. Tang, E. Sanville, G. Henkelman, *J. Phys.: Condens. Matter*, 2009, **21**, 084204.

[7] V. Wang, N. Xu, J.-C. Liu, G. Tang, W.-T. Geng, *Comput. Phys. Commun.*, 2021, **267**, 108033.

[8] A. Pandey, A. Mukherjee, S. Chakrabarty, D. Chanda, S. Basu, *ACS Appl. Mater. Interfaces*, 2019, **11**, 42094-42103.

[9] G. Zhao, K. Rui, S.X. Dou, W. Sun, *Adv. Funct. Mater.*, 2018, **28**, 1803291.

[10] C. C. McCrory, S. Jung, I. M. Ferrer, S. M. Chatman, J. C. Peters and T. F. Jaramillo, *J. Am. Chem. Soc.*, 2015, **137**, 4347-4357.

[11] C. C. McCrory, S. Jung, J. C. Peters and T. F. Jaramillo, *J. Am. Chem. Soc.*, 2013, **135**, 16977-16987.

[12] Y. Cheng, S. Lu, F. Liao, L. Liu, Y. Li, M. Shao, *Adv. Funct. Mater.*, 2017, **27**, 1700359.

[13] X. Meng, C. Ma, L. Jiang, R. Si, X. Meng, Y. Tu, L. Yu, X. Bao, D. Deng, *Angew. Chem. Int. Edit.*, 2020, **59**, 10502-10507.

[14] L. Mei, X. Gao, Z. Gao, Q. Zhang, X. Yu, A.L. Rogach, Z. Zeng, *Chem. Commun.*, 2021, **57**, 2879-2882.

[15] Z. Luo, Y. Wang, X. Wang, Z. Jin, Z. Wu, J. Ge, C. Liu, W. Xing, *ACS Appl. Mater. Interfaces*, 2019, **11**, 39782-39788.

[16] J. Liu, Y. Zheng, D. Zhu, A. Vasileff, T. Ling, S.-Z. Qiao, *Nanoscale*, 2017, **9**, 16616-16621.

[17] Y. Xu, X. Jiang, G. Shao, H. Xiang, S. Si, X. Li, T.S. Hu, G. Hong, S. Dong, H. Li, Y. Feng, S. Liu, *Energy Environ. Mater.*, 2021, **4**, 117-125.

[18] L. Ji, P. Yan, C. Zhu, C. Ma, W. Wu, C. Wei, Y. Shen, S. Chu, J. Wang, Y. Du, J. Chen, X. Yang, Q. Xu, *Appl. Catal. B Environ.*, 2019, **251**, 87-93.

[19] R. Bar-Ziv, P. Ranjan, A. Lavie, A. Jain, S. Garai, A. Bar Hen, R. Popoyitz-Biro,

R. Tenne, R. Arenal, A. Ramasubramaniam, L. Lajaunie, M. Bar-Sadan, *ACS Appl. Energy Mater.*, 2019, **2**, 6043-6050.

[20] W. Wu, C. Niu, C. Wei, Y. Jia, C. Li, Q. Xu, *Angew. Chem. Int. Edit.*, 2019, **58**, 2029-2033.